

Rationalizing acid zeolite performance at the nanoscale by correlative fluorescence and electron microscopy

Jordi Van Loon, Kris P.F. Janssen, Thomas Franklin, Alexey V. Kubarev, Julian A. Steele, Elke Debroye, Eric Breynaert, Johan A. Martens, and Maarten B.J. Roeffaers

ACS Catal., **Just Accepted Manuscript** • Publication Date (Web): 22 Jun 2017

Downloaded from <http://pubs.acs.org> on June 23, 2017

Just Accepted

“Just Accepted” manuscripts have been peer-reviewed and accepted for publication. They are posted online prior to technical editing, formatting for publication and author proofing. The American Chemical Society provides “Just Accepted” as a free service to the research community to expedite the dissemination of scientific material as soon as possible after acceptance. “Just Accepted” manuscripts appear in full in PDF format accompanied by an HTML abstract. “Just Accepted” manuscripts have been fully peer reviewed, but should not be considered the official version of record. They are accessible to all readers and citable by the Digital Object Identifier (DOI®). “Just Accepted” is an optional service offered to authors. Therefore, the “Just Accepted” Web site may not include all articles that will be published in the journal. After a manuscript is technically edited and formatted, it will be removed from the “Just Accepted” Web site and published as an ASAP article. Note that technical editing may introduce minor changes to the manuscript text and/or graphics which could affect content, and all legal disclaimers and ethical guidelines that apply to the journal pertain. ACS cannot be held responsible for errors or consequences arising from the use of information contained in these “Just Accepted” manuscripts.



1
2
3
4
5
6
7 Rationalizing acid zeolite performance at the
8
9
10
11 nanoscale by correlative fluorescence and electron
12
13
14
15 microscopy
16
17
18
19
20

21 *Jordi Van Loon,[†] Kris P. F. Janssen,[‡] Thomas Franklin,[†] Alexey V. Kubarev,[†] Julian A. Steele,[†]*
22
23 *Elke Debroye,[‡] Eric Breyneart,[†] Johan A. Martens,[†] Maarten B. J. Roeffaers^{*†}*
24
25

26 [†]Center for Surface Chemistry and Catalysis, Faculty of Bioscience Engineering, KU Leuven,
27
28 3001 Heverlee, Belgium and [‡]Department of Chemistry, Faculty of Sciences, KU Leuven, 3001
29
30 Heverlee, Belgium
31
32
33
34

35 ABSTRACT
36
37
38

39 The performance of zeolites as solid acid catalysts is strongly influenced by the accessibility of
40
41 active sites. However, synthetic zeolites typically grow as complex aggregates of small
42
43 nanocrystallites rather than perfect single crystals. The structural complexity must therefore play
44
45 a decisive role in zeolite catalyst applicability. Traditional tools for the characterization of
46
47 heterogeneous catalysts are unable to directly relate nanometer scale structural properties to the
48
49 corresponding catalytic performance. In this work, an innovative correlative super-resolution
50
51 fluorescence and scanning electron microscope is applied and the appropriate analysis
52
53 procedures are developed to investigate the effect of small-pore H-mordenite (H-MOR)
54
55
56
57
58
59
60

1
2
3 morphology on the catalytic performance, along with the effects of extensive acid leaching.
4
5 These correlative measurements revealed catalytic activity at the interface between intergrown
6
7 H-MOR crystallites that was assumed inaccessible, without compromising the shape selective
8
9 properties. Furthermore, it was found that extensive acid leaching led to an etching of the
10
11 originally accessible microporous structure, rather than the formation of an extended mesoporous
12
13 structure. The associated transition of small-pore to large-pore H-MOR therefore did not render
14
15 the full catalyst particle functional for catalysis. The applied characterization technique allows a
16
17 straightforward investigation of the zeolite structure-activity relationship beyond the single-
18
19 particle level. We conclude that such information will ultimately lead to an accurate
20
21 understanding of the relationship between the bulk scale catalyst behavior and the nanoscale
22
23 structural features, enabling a rationalization of catalyst design.
24
25
26
27
28
29
30

31 KEYWORDS

32
33
34 Zeolite catalysis, mordenite, dealumination, structure-activity relationship, super-resolution
35
36 microscopy, single-molecule fluorescence microscopy, integrated fluorescence and electron
37
38 microscope
39
40
41

42 **Introduction**

43
44 Zeolites are widely used as solid acid catalysts in both laboratory-scale research and industrial
45
46 chemical processes.^{1,2,3} Their catalytic activity and chemoselectivity are strongly influenced by
47
48 the accessibility of individual active sites that are located within the characteristic ordered
49
50 microporous structure.⁴ Structural imperfections such as defects and meso- and macropores are
51
52 therefore believed to be key determinants of catalyst performance.^{5,6} This is specifically true for
53
54 zeolites with unidirectional pore systems, such as mordenites (MOR). The MOR framework
55
56
57
58
59
60

1
2
3 consists of 12- and 8- membered ring channels running along the crystallographic c-axis and a
4 network of side pockets oriented along the b-axis that are not effectively interconnecting the
5 pores along the c-axis.⁷ Since molecular transport of most organic molecules can only occur
6 through the 7.0 Å × 6.5 Å sized 12-membered ring (12MR) channels, the MOR framework
7 porosity can be regarded as unidirectional. As a consequence, molecular diffusion is easily
8 obstructed and as-synthesized mordenite crystals therefore often display restricted mass
9 transport.⁸ According to literature, this so-called small-port (SP) behavior is most probably
10 caused by crystallographic stacking faults or extra-framework aluminum species deposited in the
11 micropores.^{7,9,10,11} The obstructed molecular accessibility in the micropores of such small-port
12 mordenites (SP-MORs) limits the catalytic activity to pore entrances located near the outer
13 surface of the crystals.⁸ These mass transport constraints are typically circumvented by applying
14 post-synthetic dealumination, such as acid leaching or hydrothermal treatments, to introduce
15 mesopores into the structure.
16
17
18
19
20
21
22
23
24
25
26
27
28
29
30
31
32
33

34 In this work, a newly developed integrated fluorescence and electron microscope (iFIEM) is
35 applied to investigate the effect of SP-MOR nanocrystallite structure on the catalytic
36 performance. The novelty of this research is two-fold. First, we describe the development of a
37 new tool that for the first time enables catalyst structure to be linked to its performance at the
38 nanoscale. The main advantages of using such an integrated instrument instead of independent
39 microscopes are the strongly reduced risk of sample contamination and that, after an initial
40 alignment of the system, structural images and catalytic activity maps are conveniently overlaid.
41 The second novelty is that, in contrast to idealized, micrometer-large crystals which have been
42 used before, this work employed a commonly applied industrial zeolite batch, containing a large
43 amount of complex intergrown particles.
44
45
46
47
48
49
50
51
52
53
54
55
56
57
58
59
60

1
2
3 The latter is of importance since most synthetic zeolite batches, including mordenites, do not
4 consist of perfect uniform crystals, but rather a wide range of particle morphologies is present. It
5
6 often follows that zeolite particles exhibit complex intergrowths and obvious structural
7
8 defects.^{11,12} The influence of this structural complexity on the catalytic performance or post-
9
10 synthetic dealumination, is not yet understood at the relevant length scales, mainly because
11
12 traditional analytical methods used in zeolite and catalysis research are unable to directly link the
13
14 effects of structural imperfections to the impact on the catalytic performance.^{4,5,12,13} Particularly
15
16 for zeolites with a one dimensional porous structure, pore blocking has a tremendous effect on
17
18 catalyst performance, but this has so far not been directly related to the local catalyst structure.¹⁴
19
20 For example, electron microscopy enables the investigation of structural details down to the
21
22 atomic scale.¹⁵ However, a direct correlation of this structurally resolved information to the
23
24 catalytic performance, which is typically measured at the bulk scale, cannot be made due to the
25
26 intrinsically large inter- and intraparticle heterogeneity. At best, the outcome of ensemble
27
28 averaged catalyst testing can lead to generalized insights on the interplay between catalyst
29
30 structure and activity.
31
32
33
34
35
36
37
38

39 Fluorescence microscopy has undeniably proven its ability to characterize and visualize the
40
41 catalytic performance down to the level of individual catalytic conversions.^{16,17} More
42
43 specifically, the optical transparency of zeolites enables the catalytic performance to be mapped
44
45 out at the nanoscale through Nanometer Accuracy by Stochastic Chemical reActions, or
46
47 NASCA,^{18,19,20} The interpretation of these spatially resolved performance maps depends on
48
49 morphological features that can typically be resolved from corresponding optical transmission
50
51 images of the same catalyst particle. This approach is therefore limited to micrometer-sized
52
53 crystals with well recognizable morphologies and structures. For example, fluorescence
54
55
56
57
58
59
60

1
2
3 microscopy investigations have led to the elucidation of the impact of intergrowth structures
4 within large H-ZSM-5 crystals on pore accessibility, chemical mobility and catalytic
5 performance.^{19,21,22} Alternatively, a number of uniform nanometer sized metal catalyst particles
6 has been investigated.^{8,23,24,25} These spatially resolved studies have so far demonstrated the
7 impact of inter- and intraparticle heterogeneities on the overall catalytic performance.²⁶ Together
8 these investigations only focused on either large, perfect crystals or relatively small particles that
9 are assumed to be uniform in size and morphology. However, this is not representative for actual
10 industrially employed catalyst powders containing non-uniform nanoparticles and complex
11 aggregates of nanocrystallites. Therefore, it is essential to correlate the nanoscale activity maps
12 recorded by NASCA microscopy to structural information of the same particle at the same length
13 scale.¹⁶

14
15
16
17
18
19
20
21
22
23
24
25
26
27
28
29 Detailed structure-activity relationships at the level of individual zeolite catalyst particles were
30 recently obtained by the Weckhuysen group by combining transmission electron microscopy
31 (TEM) with diffraction-limited wide-field fluorescence microscopy.^{27,28} While very powerful,
32 these static experiments are focused on investigating prestained samples and do not enable super-
33 resolution imaging of the catalytic activity at the nanoscale. Furthermore, care has to be taken
34 not to compromise the local catalyst structure during the sample slicing prior to the experiment.
35 Peng Chen and co-workers alternatively employed correlative fluorescence microscopy and
36 scanning electron microscopy (SEM) to link catalytic activity to the structure of metal
37 nanoparticles.^{24,29,30}

38
39
40
41
42
43
44
45
46
47
48
49
50
51 This brief summary of earlier efforts to investigate the catalyst structure-activity relationship
52 down to the nanoscale illustrates the relevance of developing an iFIEM approach as applied in
53 the reported work. By linking nanoscale catalyst performance and structure, we uncover the
54
55
56
57
58
59
60

1
2
3 significance of crystal intergrowths that induce extra-framework porosity and their role on
4 catalyst performance before and after acid leaching. Furthermore, it was discovered that there is
5
6 no significant mesopore creation through extensive acid leaching, demonstrating the need for an
7
8 additional hydrothermal treatment in order to truly circumvent the small-pore behavior of MOR
9
10 zeolites.
11
12

13 14 15 **Experimental methods**

16
17
18 **Integrated fluorescence and electron microscope.** The iFLEM setup consists of an inverted
19 epifluorescence wide-field microscope integrated into an SEM (FEI Quanta 250 FEG), by means
20 of a customized chamber door (SECOM, Delmic BV) (Figure 1).^{31,32} On the outside of the
21 sample chamber, a 532 nm diode pump solid state laser (Omicron laserage) is directed through
22 the chamber window by means of a 442/532 nm dichroic mirror with accompanying excitation
23 filter (Figure 1b). A 100× 1.4NA CFI plan APO VC oil objective lens (Nikon) located inside the
24 vacuum chamber provides the wide field excitation of the sample. As such, this system provides
25 1.9 kW.cm⁻² of excitation light on the sample. To operate the system under vacuum conditions
26 (approximately 1×10⁻⁴ Pa), 1-Ethyl-3-methylimidazolium acetate is applied as immersion liquid.
27 The generated fluorescence is guided through the optically transparent window and passes
28 through the dichroic mirror and a 542 nm LP emission filter, followed by a 2.5× camera lens in
29 front of the EMCCD camera (Hamamatsu C9100-23B). The optically transparent chamber
30 window is key to the functioning of the integrated system as it allows fluorescence and excitation
31 light to travel through the chamber door. Hence, after venting the system, catalytic activity
32 mapping can be started immediately. The described configuration provides a 32.8 × 32.8 μm²
33 field of view and a 64 × 64 nm² pixel size on the investigated sample. Wide-field fluorescence
34 movies were acquired with 30 ms exposure time. The linear polarized light experiments are
35
36
37
38
39
40
41
42
43
44
45
46
47
48
49
50
51
52
53
54
55
56
57
58
59
60

performed after introducing a Glan-Thompson polarizer (Thorlabs) into the optical pathway before the dichroic mirror. A detailed schematic representation of the iFIEM is provided in the supporting information (Scheme S1).

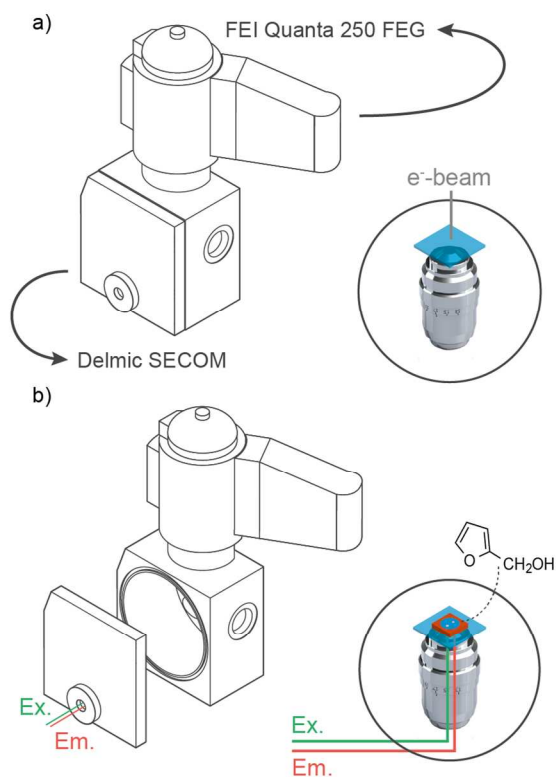


Figure 1: Schematic representation of the iFIEM showing the chamber window that is fitted into the customized SEM chamber door and is essential to the presented approach. The design is based on the SECOM platform (Delmic B.V.). Both subimages also show an inside view of the electron beam/sample/objective lens configuration in the situation that a) a structural image is being acquired with SEM and b) the single turnover precise catalytic activity map is obtained after bringing the sample to atmospheric pressure, attaching a perfusion chamber to the cover slide and adding the reagent solution.

1
2
3
4
5
6
7
8
9
10
11
12
13
14
15
16
17
18
19
20
21
22
23
24
25
26
Sample preparation. The SP-MOR sample was obtained from Tosoh Corporation (HSZ-620HOA, Si/Al ratio: 7.5). Two droplets of a 10 mg/ml mordenite in Milli Q water suspension were spin-coated onto single-molecule clean cover slides at 3000 rpm for 60 s. These single-molecule clean 22 x 22 #1 cover slides were prepared by calcination for over 24 h in a static air oven at 450 °C, followed by a 1 h ozone treatment in a UV-reactor (Ultra violet products, PR-100). The spin-coated samples were additionally calcined in a static air oven at 450 °C to remove any impurities that could lead to residual fluorescence in the zeolite sample. To ensure that no structural changes were induced in the sample, a stepwise heating scheme was used (Heating ramp of 1 °C/min and a 1 h dwell time at 80 °C and 150 °C, at 450 °C the temperature was held for at least 48 h).

27
28
29
30
31
32
33
34
35
36
37
38
39
40
41
42
43
44
45
46
47
48
49
50
51
52
53
54
55
56
57
58
59
60
Correlated data acquisition. The correlated NASCA experiments were always performed in a similar fashion. The prepared cover slide was attached onto a metal plate sample holder and mounted into the iFIEM. SEM images of the crystals were taken (2 kV, SE, high vacuum mode) (Figure 1a) after which the sample chamber of the SEM was vented to atmospheric pressure and the chamber door was opened (Figure 1b). Next, a perfusion chamber (PC8R-1.0-CoverWell, Grace Bio labs) was attached onto the cover slide and 50 µl of an 18 wt% FFA (Sigma Aldrich, 98%, purified through vacuum distillation prior to use) solution in Milli Q water was added with a micropipette. Through a set of experiments with varying concentrations, this amount was established as the optimal concentration. The addition of FFA as the fluorogenic reagent leads to the formation of oligomeric reaction products, by means of the acid-catalyzed condensation reaction that is catalyzed on the Brønsted acid sites of the zeolite (Scheme S2).¹⁷ These oligomers are composed of a conjugated backbone structure that provides the fluorescent properties to enable their observation in fluorescence experiments with single-molecule

1
2
3 sensitivity.¹⁹ In the NASCA experiment conducted on the acid leached sample, a reduced 8 wt%
4 FFA in Milli Q water solution was added to ensure the single-molecule sensitivity for this
5 catalytically more active sample. For our experiments, only crystals that show little or no
6 background fluorescence were used.
7
8
9

10
11
12 **NASCA analysis.** By fitting the point spread function of single emitters with a two-
13 dimensional Gaussian function, their exact location is determined. The localizer software used to
14 perform this analysis on the recorded fluorescence movies and produce the quantitative activity
15 maps, is available online (<https://bitbucket.org/pdedecker/localizer>) as a plugin for both Igor Pro
16 (Wavemetrics) and Matlab (MathWorks).³³ The resolution achieved by this approach is
17 approximately 20 nm.¹⁹ Single fluorescent product molecules reappearing in consecutive frames
18 before photobleaching were counted as one catalytic event. The software has a built-in
19 consolidation functionality that finds reappearing molecules within a certain distance, allowing a
20 certain blinking time. For this specific experiment, a respective distance of 50 nm and blinking
21 time of 90 ms were employed. All the parameters mentioned above were obtained after a careful
22 evaluation of different combinations of the different parameters. The quantitative NASCA
23 images that result from this analysis are obtained by binning the data into $50 \times 50 \text{ nm}^2$ areas. By
24 additionally considering the imaging depth as a measure for the thickness of every voxel, *i.e.* 500
25 nm, the corresponding catalytic activity is obtained, which is represented by assigning a color
26 scale to the resulting activity map.
27
28
29
30
31
32
33
34
35
36
37
38
39
40
41
42
43
44
45
46
47

48 **The overlay procedure.** The correlated micrographs shown in Figures 2, 3 and 4 were created
49 using the image registration tool available in ImageJ. By selecting the same two reference points
50 on both the qualitative activity map (produced using the localizer software) and the electron
51 micrograph, the correct magnification, rotation and translation is obtained that is needed to
52
53
54
55
56
57
58
59
60

1
2
3 accurately overlay both images. By merging the resized qualitative activity map and the electron
4 micrograph with the merge channels command, the correlated micrograph is obtained. The cyan
5 colored dots displayed on the SEM micrographs in this work represent the position where at least
6 one turnover has taken place.
7
8
9
10
11

12 **Molecular size calculation.** The molecular diameters of FFA and pyridine were calculated
13 using MarvinSketch (version 15.9.21.0), developed by ChemAxon.
14
15
16

17 **Reaction-pore confinement analysis.** The Matlab analysis procedure that has been developed
18 to perform the reaction-pore confinement analysis is available online
19 (<https://drive.google.com/open?id=0ByLzCpEAweEkbTdhQllxeUlzRkE>). In this analysis, the
20 NASCA image data obtained from analyzing the respective linear polarized light experiments,
21 using the localizer software and binning them into $200 \times 200 \text{ nm}^2$ zones, are used as input. The
22 two separate data sets are carefully screened for drift using a built-in drift check function. The
23 reaction-pore confinement plot in Figure 3e has been drift corrected for + 64 nm along the Y
24 axis. No drift correction was needed to obtain the reaction-pore confinement plot of the HNO₃
25 leached sample. A second parameter is set as the lower limit (LL). As such, any bins in the
26 image only composed of fluorescent background molecules are filtered out. The lower limit for
27 the analysis of the performed experiments is set to 5 turnovers. Finally, an upper threshold is set
28 for the transparency range that qualitatively displays the number of turnovers detected within the
29 respective bins. The threshold is set at 10% of the maximal bin value obtained by summing the
30 turnovers of both linear polarized light experiments in every bin.
31
32
33
34
35
36
37
38
39
40
41
42
43
44
45
46
47
48
49

50 **Acid leaching.** Dealumination has been achieved by refluxing 1 g of the SP-MOR zeolite
51 sample at 90 °C for 8 h using 20 ml of a 1 M HNO₃ (Sigma-Aldrich, 65%) in MilliQ solution
52 while vigorously stirring the slurry. The acid leached zeolite was separated from the acidic
53
54
55
56
57
58
59
60

1
2
3 solution by means of Büchner-filtration using warm distilled water until the permeate obtained a
4 neutral pH. Finally, the zeolite was dried in a static air oven for 24 h at 85 °C.
5
6

7
8 **Bulk scale characterization.** Elemental analysis of the HNO₃ leached sample has been
9 performed using ICP-OES (Varian 720-ES). N₂-adsorption isotherms have been obtained at -196
10 °C (Micromeritics 3Flex 3400 physisorption instrument). The reference and HNO₃ treated
11 samples have been degassed prior to the experiment for 4 h at 250 °C under vacuum conditions
12 (1 Pa). The specific surface area has been obtained by BET-analysis. ²⁷Al spectra were acquired
13 on a Bruker 500 MHz spectrometer, spinning the sample at 10 kHz at the magic angle. The
14 spectra were recorded using a one pulse sequence with pi/12 pulses of 2.90 μs using a recycle
15 delay of 0.8 s and referenced to a solution of 0.5 M Al(NO₃)₃ dissolved in 0.5 M HNO₃. Each
16 spectrum was acquired with 1024 scans using a spectral width of 19607 Hz recorded with a 2048
17 point FID size and processed with a 5 Hz apodization.
18
19
20
21
22
23
24
25
26
27
28
29
30
31

32 **Bulk scale reactivity testing.** The bulk scale naphthalene isopropylation reaction was
33 performed in the liquid phase using a high-pressure 15 ml TOP reactor for 8 h at 200 °C and
34 under 2 × 10⁶ Pa of N₂ gas (99.999%). A figure of the apparatus was added to the supporting
35 information (Figure S1). The reaction mixture consisted of 1.84 mmol naphthalene (Sigma-
36 Aldrich, ≥ 99%), 4 mmol 2-propanol (Biosolve ≥ 99.8%), 9 ml cyclohexane (Sigma-Aldrich, ≥
37 99.8%) and 100 mg of the MOR catalyst. The catalyst powder is used as provided by the
38 manufacturer or as obtained after acid leaching, *i.e.* crystal size 1-3 μm and average particle size
39 18 μm. After 8 h of reaction the reactor was cooled by placing it in an ice bath. The reaction
40 mixture was analyzed using a gas chromatograph (Shimadzu, CP-Sil 8, FID detector) in split
41 injection mode (split ratio 20) using N₂ carrier gas. After injection, the temperature was
42 programmed as follows: 5 min hold at 40 °C, heating to 280 °C at 4 °C/min and finally a 10 min
43
44
45
46
47
48
49
50
51
52
53
54
55
56
57
58
59
60

1
2
3 holding time. 2 mmol n-tetradecane (TCI, $\geq 99\%$) was added as internal standard for quantitative
4 gas chromatography (GC) analysis. Identification of the compounds was carried out using gas
5 chromatography-mass spectrometry.
6
7
8
9

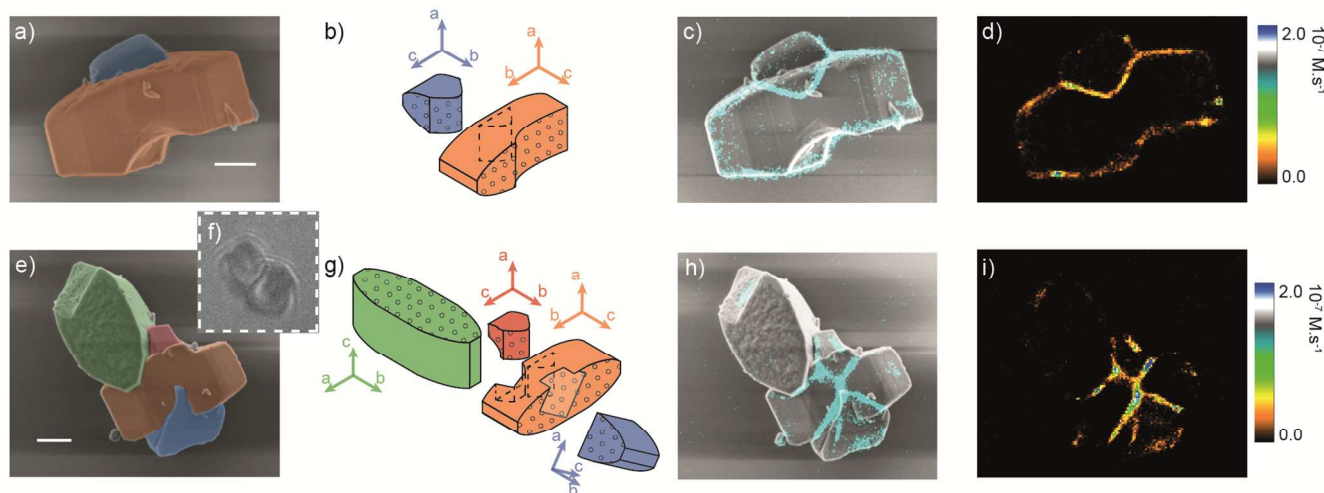
10 **Pyridine staining.** Prior to pyridine adsorption, the mordenite sample is dropcasted and
11 calcined as described in the sample preparation paragraph. After calcination, the cover slides,
12 that are contained in glass vials, are cooled down to approximately 280 °C. At this point two
13 droplets of pyridine (Sigma Aldrich, $\geq 99\%$) are pipetted onto the bottom of the vial, the glass
14 vial is closed using its lid and the sample is left for several hours for the adsorption to take place.
15
16
17
18
19
20
21

22 **Raman experiments.** The Raman experiments were performed using a Zeiss 100x 1.3 NA oil
23 immersion objective lens and a Coherent argon-ion gas laser, tuned to operate at 488 nm. This
24 resulted in a spot size of approximately 460 nm and a spatial resolution of approximately 230
25 nm, used to probe intergrown particles at discrete locations. The micro-probe power density used
26 was 15 kW.cm⁻², which is well below the damage threshold limit. The relative amount of
27 pyridine adsorbed at the different positions in the different samples is quantified by determining
28 the ratio of the pyridine to mordenite band intensity from the Raman spectra.
29
30
31
32
33
34
35
36
37
38

39 **Results and discussion**

40 Using the iFIEM approach, detailed electron micrographs of the H-MOR catalyst particle at
41 study are collected from the top of the sample and linked to catalytic activity maps of the same
42 catalyst particle obtained from the bottom-side of the sample (Figure 1). The latter is achieved by
43 measuring single catalytic turnovers using the fluorescence microscope after addition of an
44 aqueous furfuryl alcohol (FFA) solution. Localization and accumulation of the individual
45 fluorescent reaction products results in nanoscale activity maps.^{17,19} Figure 2a shows a typical
46 scanning electron micrograph of an intergrown crystal in an industrial H-MOR batch, which
47
48
49
50
51
52
53
54
55
56
57
58
59
60

1
2
3 mainly contains aggregated SP-MOR crystals. The corresponding schematic representation is
4 presented in Figure 2b. The different MOR crystals that make up the aggregate are pseudo-
5 colored as a guide for the eye and to simplify the later discussion. Here, the small blue H-MOR
6 crystal protrudes the larger orange crystal and at the opposite side a large defect is present.
7 Judging from the shape of the defect, it likely results from another intergrown crystallite that has
8 broken off. After this detailed morphological characterization, FFA was added to the SP-MOR
9 cluster, enabling the visualization of single acid-catalyzed turnovers by recording the fluorescent
10 FFA oligomer formation. The individual fluorescent reaction products were subsequently
11 localized with nanometer precision and their locations (cyan dots) overlaid with the high-
12 resolution SEM image, as shown in Figure 2c. Since the optical focus was centered around the
13 middle of the aggregate, the recorded catalytic events originate from an optical slice around the
14 center of the aggregate of approximately 500 nm thick (Scheme S1). This is also apparent from
15 the location of the recorded catalytic events with respect to the scanning electron micrograph.
16
17
18
19
20
21
22
23
24
25
26
27
28
29
30
31
32
33
34



35
36
37
38
39
40
41
42
43
44
45
46
47
48
49
50
51
52
53
54
55
56
57
58
59
60
Figure 2: Images recorded using the iFIEM of two intergrown SP-MOR particles. (a, e) Pseudo-colored scanning electron micrographs of intergrown crystallites and (b, g) the corresponding schematic representations indicating the different crystallographic axes. The (001) facets, where

1
2
3 the 12MR channels surface, are marked by the dotted pattern indicating the 12MR pore entrances
4
5 (For the original images, see Figures S2 and S3). (c, h) Overlay images of the detected individual
6
7 fluorescent products (cyan dots) on the scanning electron micrographs, referred to as correlative
8
9 micrographs and (d, i) the quantitative NASCA images obtained by binning the turnovers in 50
10
11 $\times 50 \text{ nm}^2$ zones. (f) Optical transmission image of the second aggregate. Scale bars: 1 micron.
12
13
14
15

16 The majority of the observed catalytic events is clustered in a zone of about 300 nm wide,
17
18 delineating the outer surface of the aggregated particle. This is indicative for small port behavior
19
20 as the size of the FFA reagent molecule should enable diffusion through the 12MR channels
21
22 (molecular diameter is about 6.1 Å) and earlier research on MFI type zeolites with a
23
24 characteristic 10MR microporous structure has additionally revealed full accessibility.^{8,17,34}
25
26 Importantly, experiments in this work are performed shortly after the addition of FFA and during
27
28 this period the catalytic activity remains constant. The observed small-port behavior is therefore
29
30 assumed to be an effect of mass transport limitations rather than pore blocking, which might
31
32 gradually occur by accumulation of oligomers. In the latter case, the catalytic activity would
33
34 decrease during the experiment. Secondly, varying numbers of turnovers are observed within the
35
36 active zone. The small port behavior becomes even clearer when looking at the NASCA image
37
38 obtained in Figure 2d by binning the measured catalytic turnovers into $50 \times 50 \text{ nm}^2$ zones, which
39
40 yields a quantitative view on the matter. In the main crystal (orange), most of the acid-catalyzed
41
42 oligomerization reactions are limited to two opposite crystal facets. Based on the
43
44 crystallographic structure, in combination with the morphology of the crystals, these slightly
45
46 curved and roughened facets are identified as the crystallographic (001) facets where the 12MR
47
48 pores are surfacing.^{8,35} This observation shows that catalytic conversions in SP-MOR are limited
49
50 to the acid sites available in the first few hundreds of nanometers behind the 12MR pore mouths.
51
52
53
54
55
56
57
58
59
60

1
2
3 At the other facets the microporous zeolite framework and, hence, the catalytically active sites,
4 are not accessible towards the FFA substrate. Note that the sparse turnovers detected at these
5 facets can be related to acid sites at the outer surface or minute crystal imperfections.
6
7 Surprisingly, also a significant number of catalytic turnovers is observed away from the outer
8 surface and inside the main crystal, in the zone underneath the intergrown crystal at the top. The
9 width of this catalytically active zone is comparable to that at the (001) facets at the crystal
10 exterior. Judging from the shape of this catalytically active area, it can be assigned to the
11 interface between the intergrown crystals, *i.e.* the highly defective area between the blue and
12 orange crystals. Note that the activity of this region is similar to that observed at the readily
13 accessible (001) facets and that no activity gradient is observed from the outside of the crystal
14 towards the most deeply buried part of the intergrowth. It can therefore be concluded that the
15 extra-framework porosity at this interface is sufficient to allow reagent molecules to readily
16 reach the active sites along the intergrowth.
17
18
19
20
21
22
23
24
25
26
27
28
29
30
31
32
33

34 Figures 2e and f display the scanning electron micrograph and optical transmission image of
35 another SP-MOR aggregate in this industrial H-MOR batch. A direct comparison clearly
36 demonstrates that the structural complexity of small particles in typical zeolite samples cannot be
37 captured by diffraction limited optical imaging. From the scanning electron micrograph, the
38 structural details of this aggregate can be resolved, with the corresponding schematic
39 representation shown in Figure 2g. The crystal at the top part (green) is a nearly complete crystal
40 with an obvious defect at the top. Again, from the shape of the defect, it seems to have resulted
41 from a broken off intergrown crystallite. Judging from the morphology of the particle (*vide*
42 *supra*) the 12MR micropores run perpendicular to the rough (001) top facet along the optical Z-
43 axis. In the center of the aggregate another large crystal (orange) is present, perpendicular to the
44
45
46
47
48
49
50
51
52
53
54
55
56
57
58
59
60

1
2
3 top (green) crystal. The 12MR pores in this crystal run parallel to the imaging plane, connecting
4
5 the curved (001) facets where two more protruding crystals (red and blue) are present. The
6
7 slightly different orientation of these two protruding crystals suggests that both are independent
8
9 of each other.
10

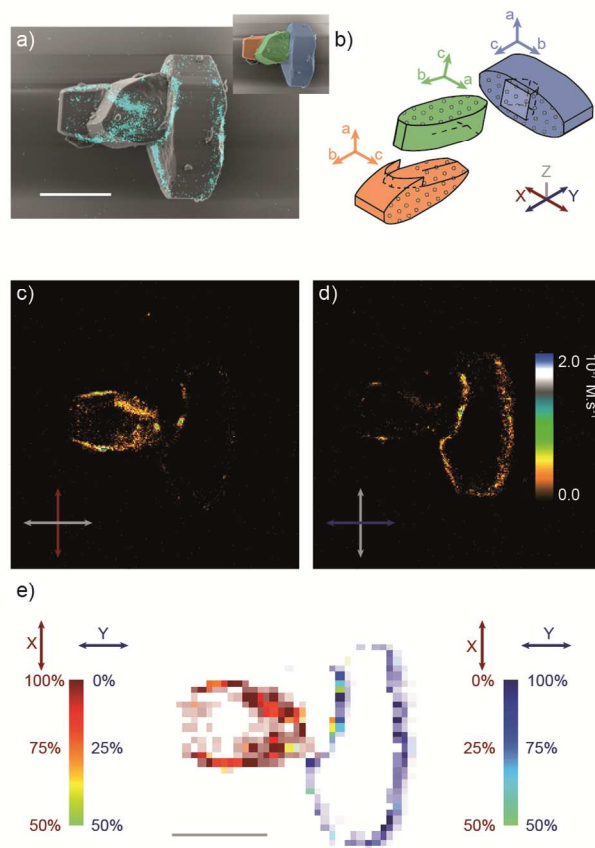
11
12 Similar to the first aggregate (Figures 2a-d), the catalytic reactivity of this particle was
13
14 measured by adding the fluorogenic FFA reagent solution and subsequently localizing the
15
16 individual catalytic turnovers. Figure 2h shows the positions of localized individual catalytic
17
18 events overlaid with the corresponding electron micrograph. The corresponding NASCA image
19
20 is shown in Figure 2i. The interface of the central crystal (orange) with the intergrown crystals
21
22 (red and blue) results in a highly active x-shaped zone of activity. Additionally, significant
23
24 catalytic activity is observed at the interface between the central (orange) and top (green)
25
26 crystals. The width of the catalytically active zones, measuring about 300 nm, and the absence of
27
28 an activity gradient within this zone is in line with earlier observations on the first aggregate. The
29
30 absence of catalytic activity in the upper (green) crystal can be explained by the orientation of
31
32 the crystal; the 12MR micropores run parallel to the propagation direction of the excitation light
33
34 (optical Z-axis). As the fluorescent product molecules are spatially constrained within the
35
36 microporous structure, the molecules will be aligned along the micropore orientation. This
37
38 results in a minimal overlap between the electric field vector of the excitation light and the
39
40 transition dipole moment of the fluorescent product molecules.^{8,36}
41
42
43
44
45
46
47

48
49 Clearly, the absence of a perfect co-alignment between the crystal lattices of the intergrown
50
51 crystals results in a local discontinuity of the zeolite framework at the boundary between these
52
53 SP-MOR crystals. The resulting extra-framework porosity facilitates molecular diffusion and
54
55 leads to an enhanced molecular accessibility. As such, this results in a zone of high catalytic
56
57
58
59
60

1
2
3 activity at the interface between the individual crystallites, away from the outer surface. The
4
5 catalytic activity at these intergrowths accounts for respectively 28 and 67% of the total catalytic
6
7 activity observed in the two examples. This data clearly underlines the importance of
8
9 intergrowths on the overall performance of these H-MOR zeolites. At the same time, these
10
11 results, showing activity away from the outer surface, also indicate that an aluminum gradient
12
13 cannot be the origin of the observed activity profile, *i.e.* active crystallite edges and inactive
14
15 crystallite center. On the other hand, it cannot be deduced from these observations whether this
16
17 catalytic activity is only linked to acid sites within the SP-MOR micropores or if some portion of
18
19 the activity is linked to defect sites at the highly defected interface. This is important, since the
20
21 latter would have a negative impact on the shape selectivity.^{37,38} Whereas product molecules
22
23 formed within the confinement of the microporous structure are expected to be aligned along the
24
25 12MR pore direction, molecules formed on active sites directly located on the highly accessible
26
27 intergrowth boundary should not show any preferential orientation.^{8,36} Hence, the orientation of
28
29 the fluorescent product molecules with respect to the one-dimensional porous structure is a good
30
31 indicator of the pore confinement, which is crucial for shape selectivity. The orientation of
32
33 fluorescent reaction products can be straightforwardly visualized by implementing linear
34
35 polarized excitation light.³⁶

36
37
38 To quantitatively investigate the pore confinement of individual fluorescent reaction products,
39
40 an aggregate of three intergrown crystals from the same SP-MOR batch was examined in Figure
41
42 3. In this cluster, the 12MR pores of the respective crystals are oriented almost perpendicular to
43
44 each other. The aggregate itself was oriented in such a way that the 12MR pores of the individual
45
46 crystals are along the optical X-, Y- and Z-axes. When exciting with circular polarized light
47
48 (Figure 3a), fluorescent oligomers oriented in the XY-plane are detected. A schematic
49
50
51
52
53
54
55
56
57
58
59
60

1
2
3 representation of the cluster in which the different axes are assigned is given in Figure 3b. As
4
5 observed in Figures 2c and h, catalytic activity is limited to zones of about 300 nm thickness
6
7 starting from the 12MR pore mouths at the (001) facets and around the intergrowth interfaces.
8
9 Note that the catalytically active zone along the interface between the middle (green) and left
10
11 (orange) crystals is broader than the previously observed 300 nm (Figures 2c and h). As the
12
13 catalytic activity map is a 2D projection of single-turnovers taking place within a 500 nm thick
14
15 optical slice (*vide supra*), the width of the projection will depend on the relative orientation of
16
17 the intergrowth structure to the optical section. Clearly, this interface does not follow any of the
18
19 crystallographic axes of the other two intergrown crystals.
20
21
22
23
24



54
55
56
57
58
59
60
Figure 3: (a) Correlative structure-activity micrograph of a cluster of three intergrown crystallites obtained with circular polarized excitation light (For the original SEM image see Figure S4) and

1
2
3 (b) the respective schematic representation with corresponding crystallographic- and optical
4 axes. Pore mouths of the 12MR are marked by the dotted pattern. The corresponding quantitative
5 activity maps (accumulated activity recorded in $50 \times 50 \text{ nm}^2$ project zones) are obtained with
6 linear polarized excitation light along the one-dimensional porous structure in (c) the left
7 (orange) crystal, *i.e.* the optical X-axis, and (d) the right (blue) crystal, *i.e.* the optical Y-axis; the
8 polarization direction is indicated by the highlighted optical axis. (e) The reaction-pore
9 confinement plot obtained by combining the information from (c) and (d), and after binning into
10 $200 \times 200 \text{ nm}^2$ areas. Scale bars: 3 microns.
11
12
13
14
15
16
17
18
19
20
21
22

23 The introduction of a Glan-Thompson polarizer into the excitation pathway of the iFIEM
24 polarizes the excitation light and can be rotated over 360° in the optical XY-plane. Next, we
25 quantitatively investigate the polarization dependence by specifically employing two
26 perpendicular polarization directions; first along the optical X-axis, parallel to the 12MR pores of
27 the orange crystal (Figure 3c), and, second, along the optical Y-axis, parallel to the 12MR pores
28 in the blue crystal (Figure 3d). This investigation reveals that the formed fluorescent product
29 molecules at the (001) facets of the respective crystals are mostly confined to their respective
30 12MR pores. When the excitation polarization is oriented along the direction of the 12MR pores
31 of the orange crystal (*i.e.* the optical X-axis), the number of catalytic turnovers observed in the
32 blue crystal reduces drastically compared to the situation in which circular polarization was
33 employed. Even though the catalytic reaction still occurs, the fluorescent product molecules are
34 no longer efficiently excited, as the polarization direction of the excitation light is perpendicular
35 to the orientation of the molecular excitation transition dipole moment. On the other hand, the
36 opposite effect is observed when the polarization plane is oriented parallel to the optical Y-axis
37 (Figure 3d). In this case, the blue crystal exhibits the majority of the catalytic activity and only a
38
39
40
41
42
43
44
45
46
47
48
49
50
51
52
53
54
55
56
57
58
59
60

1
2
3 fraction remains excitable and detectable in the orange crystal. Surprisingly, the same
4
5 observation holds for the fluorescent product molecules formed at the intergrowth regions of the
6
7 two crystals with the middle green crystal. As the 12MR pores of the latter crystal are oriented
8
9 along the optical Z-axis, no significant contribution to the catalytic activity map is expected from
10
11 the molecules confined within the microporous structure. Therefore, this is direct proof of the
12
13 pore-confinement of reaction products near crystalline defect such as intergrowth interfaces.
14
15

16
17 Combining the information from Figures 3c and d into one reaction-pore confinement plot
18
19 shows the local orientation of product molecules with respect to the 12MR pores: red-to-green
20
21 and blue-to-green color scales are indicative of a transition from a situation in which all
22
23 fluorescent product molecules are confined within the 12MR pores in the orange and blue
24
25 crystals, respectively, to a situation where there is no preferential orientation (green) (Figure 3e).
26
27 The color intensity of each pixel provides a qualitative indication of the relative number of
28
29 turnovers occurring in this zone. The reaction-pore confinement plot resulting from the aggregate
30
31 in Figure 3 mainly shows red and blue zones, corresponding to a confinement of approximately
32
33 86% over the whole particle. This value is obtained by determining the ratio of the number of
34
35 fluorescent product molecules oriented along the local microporous structure, to the total number
36
37 of catalytic turnovers observed over the catalyst particle. As such, this number represents the
38
39 shape selectivity of the individual catalyst particle based on the FFA probe reaction.
40
41
42
43
44
45

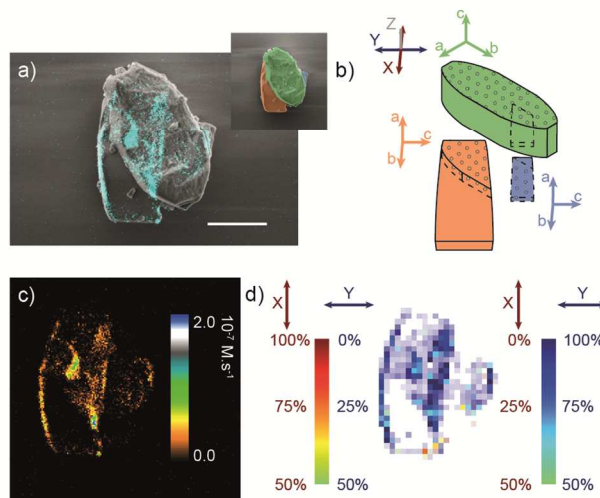
46
47 The reaction-pore confinement determined during this experiment reveals that active sites are
48
49 predominantly confined within the microporous structure as reaction products are preferentially
50
51 oriented along the one-dimensional 12MR pores. However, catalytic activity is observed on all
52
53 intergrowth structures, regardless of the crystallographic facets that are included. The formation
54
55 of the crystallographic surface is therefore assumed to be incomplete where intergrowth
56
57
58
59
60

1
2
3 formation has taken place. This leads to an opening up of the microporous structure.
4
5 Additionally, active sites accessible through intergrowth structures are as reactive as those
6
7 accessible through the intrinsic pore mouths on the (001) facets. This is an indication that mass
8
9 transport inside intergrowths is unrestricted. As such, intergrowth structures are regarded as
10
11 microporous voids that facilitate mass transport towards catalytically active sites located within
12
13 the opened up crystallographic framework.
14
15

16
17 One method commonly applied to enhance molecular transport in SP-MOR catalysts is acid
18
19 leaching, removing both framework and extra-framework aluminum species hindering molecular
20
21 transport along the 12MR pores. Already in 1983, Raatz *et al.* reported that selective leaching of
22
23 about 20% of the total aluminum content converts SP-MOR into the large-pore form.¹⁰ Since
24
25 then, such post-synthetic treatments have become routine practice in H-MOR catalytic
26
27 research.³⁹ The sample under investigation in this study was submitted to acid leaching by
28
29 refluxing the SP-MOR zeolite sample in a HNO₃ solution.⁴⁰ Typically, the effect of this
30
31 procedure on the zeolite and its catalytic performance is investigated by means of bulk-scale
32
33 analysis, such as atomic spectroscopy to determine bulk Si/Al ratio, or solid state nuclear
34
35 magnetic resonance (NMR) to discriminate between framework (Al^{IV}) and extra-framework
36
37 aluminum (Al^{VI}). Here, bulk analysis using inductively coupled plasma optical emission
38
39 spectrometry (ICP-OES) revealed that about 30% of the aluminum was removed from the zeolite
40
41 sample and ²⁷Al NMR data additionally showed a slight preference towards extra-framework
42
43 Al^{VI} removal. N₂-physisorption revealed a small increase in micropore- and external surface
44
45 area. Finally, also a bulk scale naphthalene isopropylation reaction was performed on the
46
47 mordenite catalysts. As such, the reactivity trends and shape selectivity properties, observed at
48
49 the single particle level, before and after acid leaching, could be validated using an industrially
50
51
52
53
54
55
56
57
58
59
60

1
2
3 relevant bulk scale process. The naphthalene isopropylation reaction revealed an increased
4 activity from < 1% conversion, to 8% after HNO₃ leaching, indicating that after the SP-MOR
5 sample indeed became more active towards the alkylation of bulky organic molecules after the
6 acid treatment. A summary of these bulk scale experiments can be consulted in the supporting
7 information.
8
9
10
11
12
13
14

15 A combination of the newly developed iFIEM approach with the analysis tools introduced
16 above provides a novel way to investigate the effects of acid leaching beyond the bulk scale.
17
18 Figure 4 reveals the reaction-pore confinement for an HNO₃ treated aggregate consisting of three
19 orthogonally intergrown crystals. The orange crystal is oriented with its 12MR pores running
20 along the optical Y-axis and the 12MR pores in the green crystal run parallel to the optical Z-
21 axis. Additionally, a smaller crystallite (blue) is intergrown with the green crystal.
22
23
24
25
26
27
28
29



30
31
32
33
34
35
36
37
38
39
40
41
42
43
44
45
46
47 Figure 4: (a) Correlative structure-activity micrograph of three intergrown crystallites treated
48 with HNO₃ obtained with circular polarized excitation light (For the original SEM image see
49 Figure S5) and (b) the respective schematic representation. The (001) facets, where the 12MR
50 channels surface, are marked by the dotted pattern. (c) The corresponding quantitative activity
51 map is obtained by using a 60% reduced fluorogenic reagent concentration compared to the
52
53
54
55
56
57
58
59
60

1
2
3 previous experiments and the recorded activity is accumulated in $50 \times 50 \text{ nm}^2$ zones. (d) The
4
5 molecular confinement plot is recorded by combining the information from the linear polarized
6
7 excitation experiments as introduced in Figure 3e and after rebinning into $200 \times 200 \text{ nm}^2$ areas.
8
9

10 Scale bar: 2 micron
11

12
13 The correlated micrograph and quantitative activity map in Figure 4a and c show that the
14
15 catalytic activity in the acid leached particle still predominantly resides at the edges of the orange
16
17 crystal and the intergrowth, between the orange and green crystals. Furthermore, there is a zone
18
19 of moderate catalytic activity in the green crystal which is attributed to the small intergrown blue
20
21 crystal. As it is located beneath the green crystal, both the morphology of this crystal and the
22
23 exact orientation of the intergrowth remain unresolved by means of SEM imaging. However,
24
25 based on the information obtained from the reaction-pore confinement plot (Figure 4d), it is fair
26
27 to assume that the orientation of the blue crystal is similar to that of the larger orange crystal.
28
29 Note that the fluorogenic reagent concentration was reduced because of the increased reactivity
30
31 over the untreated H-MOR sample (Figure S7). This increased reactivity is in line with the
32
33 results from the bulk scale naphthalene isopropylation reaction. Additionally, the reaction-pore
34
35 confinement plot in Figure 4d only reveals a slightly reduced molecular confinement of 83%.
36
37 These results further confirm the earlier assumption that the formation of intercrystalline
38
39 intergrowths lead to a locally enhanced access to the microporous structure. The effect of the
40
41 acid treatment would otherwise be much more effective if the intergrowths existed of combined
42
43 micro-, meso-, and macroporous regions.
44
45
46
47
48
49
50

51 The presented nanoscale structure-activity experiments are a representative subset of a larger
52
53 number of experiments ($n = 10$) and reveal that the location of the catalytic activity in H-MOR
54
55 zeolites is not dramatically influenced by typical acid leaching. In earlier research, Liu *et al.*
56
57
58
59
60

1
2
3 demonstrated that severe dealumination, removing more than 50% of the framework aluminum,
4 was necessary to render the full catalyst particles accessible.⁸ In their work, dealumination was
5 achieved by means of a combined hydrothermal and acid treatment. Where acid leaching mainly
6 enhances the local reactivity by etching the easily accessible microporous structure, the
7 hydrothermal treatment introduces extensive meso- and macoporous defects that render the full
8 catalyst particle accessible.
9

10
11 Intergrowth structures are affected to the same extent as the intrinsically active edges of the
12 crystals, despite the former being much more defected. Even though over 30% of the aluminum
13 has been removed, the H-MOR still displayed the typical reaction distribution and shape
14 selective properties associated with small-pore behavior, and therefore no transition from small-
15 pore to large-pore H-MOR seemed to have taken place. Small- or large-pore behavior is typically
16 revealed by performing static benzene uptake experiments,^{9,10} pyridine adsorption has been
17 investigated using Raman spectroscopy to mimic such static experiments and confirm our
18 findings based on the FFA oligomerization reaction. This approach involves the investigation of
19 pyridine uptake before and after acid leaching in targeted areas of an intergrown particle; the
20 crystallite edge, center and on the interparticle intergrowth. The results are shown in the
21 supporting information (Figure S8 and Table S4).
22
23

24 The pyridine uptake experiments indeed show an opening up of the microporous network and
25 thus a transition of small-pore to large-pore H-MOR, even though pyridine is a bulkier molecule
26 than the FFA reagent (molecular diameter for pyridine is about 6.7 Å). This significantly
27 increased pyridine uptake in all three selected areas of the acid leached particle seems to
28 contradict the outcome of the NASCA experiments. The discrepancy between both experiments
29 can be explained by the dynamic aspect of the NASCA experiments in which molecular transport
30
31
32
33
34
35
36
37
38
39
40
41
42
43
44
45
46
47
48
49
50
51
52
53
54
55
56
57
58
59
60

1
2
3 also plays a significant role. On the contrary, the pyridine distribution is determined after
4 reaching equilibrium. Hence, we believe that the fluorogenic reaction gives a more accurate
5 picture of the catalytically relevant domains. Alternatively, the presented observations could be
6 interpreted as being an effect of Al zoning, however, this effect has not been reported for the
7 MOR sample.⁸

15 **Conclusions**

16
17 In conclusion, the catalytic performance of acid zeolite nanocrystallites was studied by linking
18 the catalytic performance, as observed in super-resolution fluorescence microscopy, to structural
19 features of the same crystallite recorded by scanning electron microscopy. This enabled, for the
20 first time, a direct observation of the effect of defects and intergrowths, commonly present in
21 powdered zeolite batches, on the overall performance. First, intercrystalline intergrowth
22 structures in SP-MOR aggregates were demonstrated to have a major contribution to the overall
23 activity. The molecular confinement plots revealed that reaction products at the defect-rich
24 intergrowth boundary preferentially align with the 12MR pores rather than taking random
25 orientations. Hence, catalytically active sites at intergrowths are mainly located within the
26 microporous structure. The intergrowth structure is therefore identified as a void space that
27 allows unrestricted mass transport, enabling reactions to occur in the adjacent micropores.
28 Secondly, dealumination by acid leaching mainly affects the intergrowths and the crystal edges.
29 Surprisingly, even though more than 30% of aluminum was removed and pyridine adsorption
30 experiments showed a transition from small-pore to large-pore H-MOR, the reactivity pattern was
31 not altered. Furthermore, a similar reaction-pore-confinement is observed on the crystal edges
32 and intergrowths, before and after acid leaching, indicating the importance of such intergrowths
33 for the overall catalyst performance. This is relevant information with the aim of rationalizing
34
35
36
37
38
39
40
41
42
43
44
45
46
47
48
49
50
51
52
53
54
55
56
57
58
59
60

1
2
3 catalyst synthesis. Full catalytic utilization of the zeolite material on the other hand requires
4
5 more severe post-synthetic treatments *e.g.* more extensive acid leaching or a combination with
6
7 hydrothermal treatment.^{8,36,41} Future research should focus on the role of intercrystalline
8
9 intergrowth structures with respect to catalyst coking and mesopore creation through
10
11 hydrothermal treatment. Additionally, this line of research would benefit from the development
12
13 of an *in-situ* liquid cell that enables truly integrated experiments, allowing the fluorogenic
14
15 reaction to be conducted within the vacuum of the SEM chamber.
16
17
18

19 ASSOCIATED CONTENT

20
21 **Supporting Information.** A scheme describing the NASCA technique, showing the optical slice
22
23 and depicting the details of the iFIEM setup, a picture of the apparatus used for the bulk
24
25 characterization, the raw SEM images of the different experiments, the bulk characterization data
26
27 of untreated- and acid leached samples, the results of an experiment on the untreated sample
28
29 using the decreased FFA concentration, transmission images of intergrown particles before and
30
31 after acid leaching loaded with pyridine indicating the areas probed with Raman and the results
32
33 of the pyridine uptake experiments. This material is available free of charge on the ACS
34
35 Publications website at <http://pubs.acs.org>.
36
37
38
39

40 AUTHOR INFORMATION

41 **Corresponding Author**

42
43 *E-mail (Maarten B. J. Roeffaers): maarten.roeffaers@kuleuven.be
44
45
46
47

48 **Author Contributions**

49
50 The manuscript was written through contributions of all authors. All authors have given approval
51
52 to the final version of the manuscript.
53
54
55
56
57
58
59
60

ACKNOWLEDGMENT

The authors acknowledge financial support from the Research Foundation-Flanders (FWO, Grant Nos. G.0962.13, and G.0197.11, postdoctoral fellowship to E.D. and K.P.F.J.), KU Leuven Research Fund (C14/15/053, OT/12/059), the Hercules foundation (HER/11/14), and the Belgian Federal Science Policy Office (IAP-VII/05). The research leading to these results has received funding from the European Research Council under the European Union's Seventh Framework Programme (FP/2007-2013)/ERC Grant Agreement no. [307523], ERC-Stg LIGHT to M.B.J.R.

REFERENCES

1. Climent, M. J., Corma, A., Iborra, S. In *Zeolites and Catalysis: Synthesis, Reactions and Applications*, 1st ed.; Cejka, J., Corma, A., Zones S., Eds.; Wiley-VCH: Weinheim, 2010.
2. Dumesic, J. A., Huber, G. W., Boudart, M. In *Handbook of Heterogeneous Catalysis*, 2nd ed.; Ertl, G., Knözinger, H., Schuth, F., Weitkamp, J., Eds.; Wiley-VCH: Weinheim, 2008.
3. Hagen, J. In *Industrial Catalysis: A Practical Approach*, 2nd ed.; Hagen, J., Ed. Wiley-VCH: Weinheim, 2006.
4. De Cremer, G.; Sels, B. F.; De Vos, D. E.; Hofkens, J.; Roefsaers, M. B. J. *Chem. Soc. Rev.* **2010**, 39, 4703–4717.
5. Janssen, K. P. F.; De Cremer, G.; Neely, R. K.; Kubarev, A. V; Van Loon, J.; Martens, J. A.; De Vos, D. E.; Roefsaers, M. B. J.; Hofkens, J. *Chem. Soc. Rev.* **2014**, 43, 990–1006.
6. Rolison, D. R. *Science* **2003**, 299, 1698–1701.
7. Meier, W. M. Z. *Kristallogr. - New Cryst. Struct.* **1961**, 115, 439–450.

- 1
2
3 8. Liu, K. L.; Kubarev, A. V.; Van Loon, J.; Uji-I, H.; De Vos, D. E.; Hofkens, J.; Roeffaers,
4 M. B. J. *ACS Nano* **2014**, 8, 12650–12659.
5
6
7
8
9 9. Freund, E.; Marcilly, C.; Raatz, F. *Chem. Soc., Chem. Commun.* **1982**, 309–310.
10
11
12 10. Raatz, F.; Marcilly, C.; Freund, E. *Zeolites* **1985**, 5, 329–333.
13
14
15
16 11. van Geem, P. C.; Scholle, K. F. M. G. J.; van der Velden, G. P. M. *J. Phys. Chem.* **1988**,
17 92, 1585–1589.
18
19
20
21 12. Buurmans, I. L. C.; Weckhuysen, B. M. *Nat. Chem.* **2012**, 4, 873–886.
22
23
24
25 13. Weckhuysen, B. M. *Chem. Soc. Rev.* **2010**, 39, 4557–4559.
26
27
28 14. Magnoux, P.; Cartraud, P.; Mignard, S.; Guisnet, M. *J. Catal.* **1987**, 106, 242–250.
29
30
31 15. Lu, J.; Roeffaers, M. B. J.; Bartholomeeusen, E.; Sels, B. F.; Schryvers, D. *Microsc.*
32 *Microanal.* **2014**, 20, 42–49.
33
34
35
36
37 16. Roeffaers, M. B. J.; Cremer, G. De; Uji-i, H.; Sels, B. F.; Jacobs, P. A.; Schryver, F. C. De;
38 Vos, D. E. De; Hofkens, J. *Proc. Natl. Acad. Sci. U. S. A.* **2007**, 104, 12603–12609.
39
40
41
42
43 17. Roeffaers, M. B. J.; Sels, B. F.; Uji-i, H.; Blanpain, B.; L'hoest, P.; Jacobs, P. A.; De
44 Schryver, F. C.; Hofkens, J.; De Vos, D. E. *Angew. Chem., Int. Ed.* **2007**, 46, 1706–1709.
45
46
47
48
49 18. Roeffaers, M. B. J.; Sels, B. F.; Uji-I, H.; De Schryver, F. C.; Jacobs, P. A.; De Vos, D. E.;
50 Hofkens, J. *Nature* **2006**, 439, 572–575.
51
52
53
54
55
56
57
58
59
60

- 1
2
3 19. Roeffaers, M. B. J.; De Cremer, G.; Libeert, J.; Ameloot, R.; Dedecker, P.; Bons, A. J.;
4
5 Bückins, M.; Martens, J. A.; Sels, B. F.; De Vos, D. E.; Hofkens, J. *Angew. Chem., Int. Ed.* **2009**,
6
7 48, 9285–9289.
8
9
10
11 20. Xu, W.; Kong, J. S.; Yeh, Y.-T. E.; Chen, P. *Nat. Mater.* **2008**, 7, 992–996.
12
13
14 21. Karwacki, L.; Stavitski, E.; Kox, M. H. F.; Kornatowski, J.; Weckhuysen, B. M. *Angew.*
15
16 *Chem., Int. Ed.* **2007**, 46, 7228–7231.
17
18
19
20 22. Tachikawa, T.; Yamashita, S.; Majima, T. *J. Am. Chem. Soc.* **2011**, 133, 7197–7204.
21
22
23 23. Ristanović, Z.; Kerssens, M. M.; Kubarev, A. V.; Hendriks, F. C.; Dedecker, P.; Hofkens,
24
25 J.; Roeffaers, M. B. J.; Weckhuysen, B. M. *Angew. Chem., Int. Ed.* **2015**, 1836–1840.
26
27
28
29 24. Zhou, X.; Choudhary, E.; Andoy, N. M.; Zou, N.; Chen, P. *ACS Catal.* **2013**, 3, 1448–
30
31 1453.
32
33
34 25. Han, K. S.; Liu, G.; Zhou, X.; Medina, R. E.; Chen, P. *Nano Lett.* **2012**, 12, 1253–1259.
35
36
37
38 26. Plessers, E.; Stassen, I.; Sree, S. P.; Janssen, K. P. F.; Yuan, H.; Martens, J.; Hofkens, J.;
39
40 De Vos, D.; Roeffaers, M. B. J. *ACS Catal.* **2015**, 5, 6690–6695.
41
42
43 27. Karreman, M. A.; Buurmans, I. L. C.; Geus, J. W.; Agronskaia, A. V.; Ruiz-Martínez, J.;
44
45 Gerritsen, H. C.; Weckhuysen, B. M. *Angew. Chem., Int. Ed.* **2012**, 51, 1428–1431.
46
47
48 28. Karreman, M. A.; Buurmans, I. L. C.; Agronskaia, A. V.; Geus, J. W.; Gerritsen, H. C.;
49
50 Weckhuysen, B. M. *Chem. - Eur. J.* **2013**, 19, 3846–3859.
51
52
53
54
55
56
57
58
59
60

- 1
2
3 29. Sambur, J. B.; Chen, T.-Y.; Choudhary, E.; Chen, G.; Nissen, E. J.; Thomas, E. M.; Zou,
4 N.; Chen, P. *Nature* **2016**, 530, 77–80.
5
6
7
8
9 30. Andoy, N. M.; Zhou, X.; Choudhary, E.; Shen, H.; Liu, G.; Chen, P. *J. Am. Chem. Soc.*
10 **2013**, 135, 1845–1852.
11
12
13
14 31. Liv, N.; Zonnevylle, A. C.; Narvaez, A. C.; Effting, A. P. J.; Voorneveld, P. W.; Lucas, M.
15 S.; Hardwick, J. C.; Wepf, R. A.; Kruit, P.; Hoogenboom, J. P. *PLoS One* **2013**, 8, 1–9.
16
17
18
19
20 32. de Boer, P.; Hoogenboom, J. P.; Giepmans, B. N. G. *Nat. Methods* **2015**, 12, 503–513.
21
22
23
24 33. Dedecker, P.; Duwé, S.; Neely, R. K.; Zhang, J. *J. Biomed. Opt.* **2012**, 17, 126008.
25
26
27
28 34. Roeffaers, M. B. J.; Ameloot, R.; Bons, A. J.; Mortier, W.; De Cremer, G.; De Kloe, R.;
29 Hofkens, J.; De Vos, D. E.; Sels, B. F. *J. Am. Chem. Soc.* **2008**, 130, 13516–13517.
30
31
32
33 35. P. Simoncic; Armbruster, T. *Am. Mineral.* **2004**, 89, 421–431.
34
35
36
37 36. Kubarev, A. V.; Janssen, K. P. F.; Roeffaers, M. B. J. *ChemCatChem* **2015**, 7, 3646–3650.
38
39
40 37. Csicsery, S. M. *Zeolites* **1984**, 4, 202–213.
41
42
43
44 38. Song, C. *Surf. Chem. Catal.* **2000**, 3, 477–496.
45
46
47 39 van Donk, S.; Janssen, A. H.; Bitter, J. H.; de Jong, K. P. *Catal. Rev.* **2003**, 45, 297–319.
48
49
50 40 Giudici, R.; Kouwenhoven, H. W.; Prins, R. *Appl. Catal., A* **2000**, 203, 101–110.
51
52
53
54 41. Nesterenko, N. S.; Thibault-Starzyk, F.; Montouillout, V.; Yuschenko, V. V.; Fernandez,
55 C.; Gilson, J. P.; Fajula, F.; Ivanova, I. I. *Microporous Mesoporous Mater.* **2004**, 71, 157–166.
56
57
58
59
60

TABLE OF CONTENTS GRAPHIC



1
2
3
4
5
6
7
8
9
10
11
12
13
14
15
16
17
18
19
20
21
22
23
24
25
26
27
28
29
30
31
32
33
34
35
36
37
38
39
40
41
42
43
44
45
46
47
48
49
50
51
52
53
54
55
56
57
58
59
60